Inverse application of artificial intelligence for the control of power converters

Yuan Gao, *Member, IEEE*, Songda Wang, *Member, IEEE*, Habibu Hussaini, *Student Member, IEEE*, Tao Yang, *Senior Member, IEEE*, Tomislav Dragicevic, *Senior Member, IEEE*, Serhiy Bozhko, *Senior Member, IEEE*, Pat Wheeler, *Fellow, IEEE* and Sergio Vazquez, *Fellow, IEEE*

***Abstract*—This paper proposes a novel application method, Inverse Application of Artificial Intelligence (IAAI) for the control of power electronic converter systems. The proposed method can give the desired control coefficients/references in a simple way because, compared to conventional methods, IAAI only relies on a data-driven process with no need for an optimization process or substantial derivations. Noting that the IAAI approach uses artificial intelligence to provide feasible coefficients/references for the power converter control, rather than building a new controller. After illustrating the IAAI concept, a conventional application method of Artificial Neural Network (ANN) is discussed, an optimization-based design. Then, a two-source-converter microgrid case is studied to choose the best droop coefficients via the optimization-based approach. After that, the proposed IAAI method is employed for the same microgrid case to quickly find good droop coefficients. Furthermore, the IAAI method is applied to a modular multi-level converter (MMC) case, extending the MMC operation region under unbalanced grid faults. In the MMC case, both simulation and experimental online tests validate the operation, feasibility and practicality of IAAI.**

***Index Terms*—Artificial intelligence (AI), Machine learning, Droop control, Power converters, Inverse application, Artificial neural network (ANN), Droop control, Current sharing.**

I. Introduction

With the rapid development of data science and computing technology, the application of artificial intelligence (AI) has been growing for a few decades [1, 2]. For AI applications in the power electronics domain, particular interests include the design and optimization of components, fault diagnosis, preventive maintenance, reliability analysis and control strategies [3-5].

AI can be implemented using pre-defined rules; but in most cases AI relies on machine learning (ML) algorithms to perform specific AI tasks via a model training process. ML algorithms can learn the rules/relations from training data and improve the trained models automatically through experience. Therefore, the largest use of AI in power electronics is with ML. Other applicable AI methods include expert systems, fuzzy logic, and metaheuristic methods [3]. To distinguish ML from the metaheuristic search algorithms, [6] proposed a simple algorithm categorization that comprises the search algorithm and the surrogate algorithm (2SA). This paper will only focus on the AI applications using ML algorithms. However, the general inverse thinking of the proposed AI application would also apply to other AI algorithms.

In [3], an overview of AI applications for power electronic systems was given where more than 500 publications were reviewed. All the related applications were generally categorized into three distinctive life-cycle phases of power electronic systems: design and optimization, control, and maintenance. According to the statistical Sankey diagram of AI applications in the three life-cycle phases (Fig. 3 in [3]), ML based classification was nearly all used for the maintenance of power electronic systems, rarely for the control; Instead, regression and optimization techniques are used for the control phase. Different ML classification methods have already been applied in the control of power electronic converter systems, for example, support vector machine [7-9] and neural network (NN) pattern recognition [10, 11]. In this paper, a novel application of AI/ML is proposed which can generally fit with both regression and classification techniques; additionally, this idea does not need an optimization process.

ML algorithms can be categorized into three main groups: supervised learning, unsupervised learning, and reinforcement learning [2, 3, 5]. According to the statistics in [3], usage of supervised learning is 91% of all ML applications for power electronics applications. Therefore, supervised learning is the main approach for ML applications in this area. In particular, the most popular implementation of such methods is based on Artificial Neural Networks (ANNs), which share some principles with biological neurons in brains [5, 12]. The main three classes of ANN are feedforward, convolutional, and recurrent NN [2, 5]. Among them, feedforward ANN is the simplest and it is a universal function approximator with strong generalization capability [13]. Therefore, this study will mainly investigate the Inverse Application (IA) method of feedforward ANNs. Different from the recurrent NN which stores past outputs as a part of inputs, the proposed IA method directly swops places of the inputs/outputs in the original system. After ANN training, the trained ANN can smoothly provide the desired coefficient or reference for the power converter control.

Advanced control methods for power electronic converters in

This work was supported by the Clean Sky 2 Joint Undertaking under the European Union's Horizon 2020 Research and Innovation Programme under Grant Agreement Number 807081.

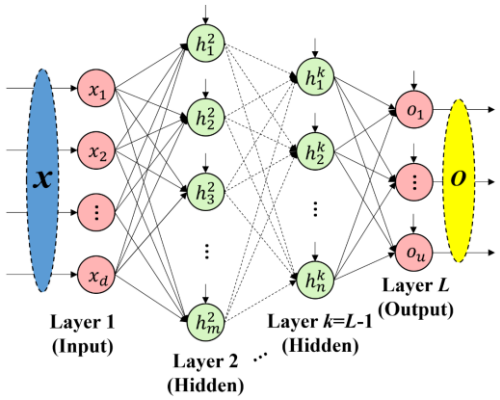

Fig. 1. Diagram of a feedforward ANN, which comprises an input layer (*x*), one or more hidden layers (*h*), and an output layer (*o*). The internal weights (ω_{ij}^{l}) and bias (b_i^{l}) terms are omitted for simplicity.

distributed generation systems and microgrids were reviewed in [14]. The control methods can be divided into model-based and data-based strategies. The first category, model-based control, considers state feedback control, sliding mode control, and model predictive control. Examples of the other category, data-based control, are ANN and fuzzy control, which are explicitly designed by using the available input/output data to do the functional approximation for system control. It is important to highlight that the key role of this paper is not using ANN to approximate/imitate a power system controller, but to provide suitable parameters (e.g., ratios, references) for the system control. By running multiple simulations to collect data, this role can be achieved by the inversely designed ANN(s).

The most commonly used approach of AI applications in power electronic systems is training ANNs offline as the surrogate models, for instance, weighting factor tuning [4], optimal design for reliability [12, 15], ANN imitation controller [10, 11, 16-19], and open-switch fault diagnosis [20]. The training data can be collected either from the real system or from a model of the actual plant. After training and validation, the surrogate models can be applied online, providing desired outputs when given suitable inputs in the operation of real system. As the ANN surrogate only involves basic algebraic operations, the process of output generation is extremely fast. Therefore, when searching for the optimal design of the studied system, an exhaustive algorithm can be used to do the optimization based on the trained ANN(s) [12, 15], the so-called optimization-based design process [21].

Most of the existed studies train the surrogate models just following the original input-output relations in power electronic systems. In contrast, this paper proposes a novel application idea, the Inverse Application of Artificial Intelligence (IAAI) method, by swopping the input-output locations (see Section III). This method can find the optimal design (or desired parameters) through a trained surrogate model but without the conventional optimization process, which should be much easier to implement. This is the main motivation for the study performed in this paper.

This paper is organized as follows. The conventional optimization-based design using ANN is illustrated in Section II. Then, in Section III, the proposed IAAI method is introduced

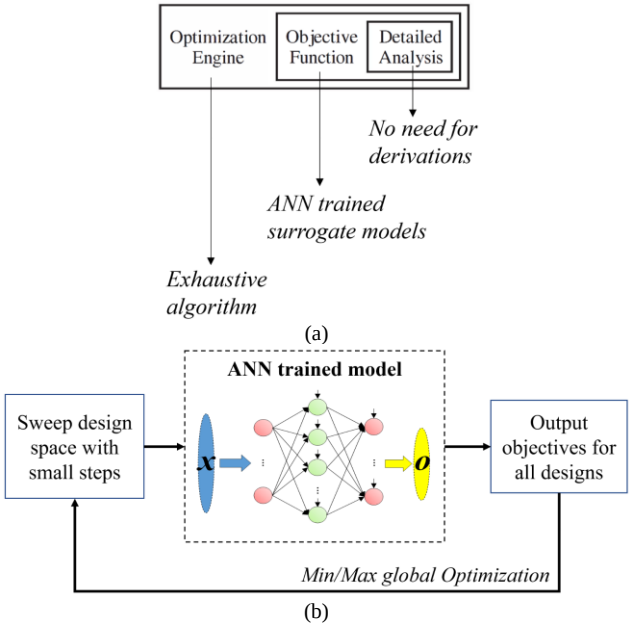

Fig. 2. Optimization-based design using ANN. (a) Three parts: detailed analysis, objective function, and optimization engine. (b) Exhaustive algorithm for the optimization using ANN

and compared to the inverse function concept. Based on that, three control cases of power converter systems are elaborated one by one for the method validation, in Section IV, V, and VI, respectively. The first case is using the conventional optimization-based design approach while the other two are based on the IAAI approach.

II. ANN Principles and Optimization-Based Design Using ANN

This section briefly introduces the fundamentals of feedforward ANN. Then, the conventional optimization-based design using ANN will be considered.

A. Feedforward ANN

Feedforward ANN is selected as the desired surrogate model in this work. Although feedforward ANN is the simplest type of ANN devised, it can demonstrate an excellent regression ability for the input-output mapping. Unlike the functional fitting (e.g., polynomial, exponential), users of feedforward ANN do not need to specify any function for this relationship mapping. It has been applied to various electrical engineering problems, from the optimal design for reliability of power electronic converters [12, 15], to the permanent-magnet motor performance correction [22, 23].

As shown in Fig. 1, a basic feedforward ANN comprises an input layer (*x*, marked in red), one or more hidden layers (*h*, marked in green), and an output layer (*o*, marked in red). Each layer has one or several artificial neurons which receive and process signal(s) from predecessor neurons, after that neurons pass the processed data to the next layer.

In a layer l (hidden layer or output layer), to calculate the output of a certain neuron n_i^l, the outputs of all the neurons p_j^{l-1} in Layer $l-1$ ($j = [1..N_{l-1}]$, N_{l-1} denotes the neuron number of Layer $l-1$) are multiplied with given weights ω_{ij}^l and then

the bias b_i^l is added. The result is further processed through an activation (propagation) function f_σ that usually takes the form of a sigmoid function, i.e. $f_\sigma(A) = 1/(1+e^{-A})$, to generate the output p_i^l. This output then becomes one of the inputs for the next layer, $l+1$, and the same procedure is repeated to calculate the output of other neurons in layer l.

In Layer 1 (input layer), p_i^1 takes the form of inputs through the neuron n_i^1. On the other side, Layer L (output layer) typically uses the linear activation function to integrate signal(s) of Layer $L-1$ for the desired output data p_i^L. In summary, the complete signal flow of ANN can be described as follows:

- Layer 1:

$$p_i^1 = x_i, i = 1,..,N_1 \quad (1)$$

where x_i are the inputs.

- Layers $l = 2,..L-1$ (hidden):

$$p_i^l = f_\sigma\left(\sum_{j=1}^{N_{l-1}} \omega_{ij}^l p_j^{l-1} + b_i^l\right), i = 1,..,N_l \quad (2)$$

- Layer L (output):

$$o_i = \omega_i^L p_i^L, i = 1,..,N_L \quad (3)$$

where o_i are the outputs.

Therefore, from inputs to outputs, feedforward ANN only involves mathematical calculations. Neuron numbers in input/output layers are determined by the training data set, but the hidden-layer neuron numbers can be set as a developer for a better regression performance. Moreover, such a general nonlinear model can approximate any given input-output function with arbitrary precision [13]. Its excellent generalization ability ensures that the trained ANN surrogate can replace the original detailed system to smoothly perform the desired tasks.

B. Optimization-Based Design Using ANN

As shown in Fig. 2(a), the optimization-based design process is conventionally illustrated by three parts: optimization engine, objective function, and detailed analysis [21]. The optimization engine is depicted at the outer level because its computational algorithm is operated on the design variables and the objective function (during all the optimization generations). The detailed analysis is the modelling basis to calculate the desired objective values and check the optimization constraints.

By using ANN, a data-driven approach, the mapping from variables to objectives can be explicitly represented by a trained ANN; thus, there is no need for substantial derivations in the original analysis module. However, in some cases, the raw data may need to be pre-processed before the ANN training. Furthermore, as mentioned, evaluation of ANN is generally very computationally light; Due to that, an exhaustive algorithm can be used as the optimization engine, which can also efficiently output the optimal design.

As shown in Fig. 2(b), after training the ANN surrogate model(s), a large number of design points can be sampled with very small steps in the design space. Then their corresponding outputs can be quickly generated via the trained ANNs. Among these input/output pairs, the optimal *min*/*max* design will be easily obtained by sorting the obtained objective values. Therefore, in a conventional way, the role of ANN model is to replace the original system and efficiently generate the objective values for an optimization problem.

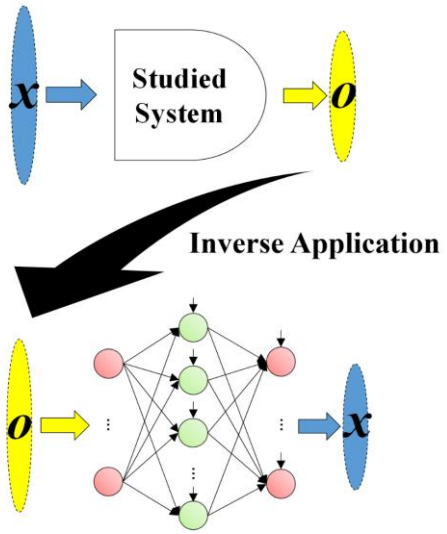

Fig. 3. Diagram of Inverse Application of Artificial Intelligence (IAAI).

III. Inverse Application of Artificial Intelligence (IAAI)

Based on the conventional application method of ANN, this section will introduce the proposed IA method of ANN. Furthermore, the differences and connections between IAAI and the inverse function will be discussed.

A. IAAI Method

ANN is based on a nonparametric function approximation model in supervised learning, purely mathematic. There is no requirement for ANN inputs and outputs. Moreover, the user does not need to specify the relationship between the predictors (input data) and responses (output data) with a predetermined regression function. This flexibility is the theoretical basis of the proposed IAAI method.

In Section II, the ANN built for conventional optimization-based design follows the original input/output relations in the studied system. However, the fact is that the desired optimal design (obtained via optimization) locates at the input layer of ANN, i.e., the logic direction of optimization-based design is from outputs to inputs [see Fig. 2(b)].

Inspired by this fact, this paper proposes to swop the locations of original inputs/outputs and build ANN(s) mapping from outputs to inputs, as shown in Fig. 3. There may be no physical or electrical meaning in this mapping but, after data collection and ANN training, the desired parameters in the studied system (e.g., ratios, references) can be directly obtained by giving just one feasible combination of original outputs (i.e., ANN inputs) without an optimization process. Therefore, the proposed IAAI method should be easier than the conventional optimization-based design approach because it deletes the optimization engine. Moreover, it has the potential to discover unknown ways to address real problems. Noting that, the

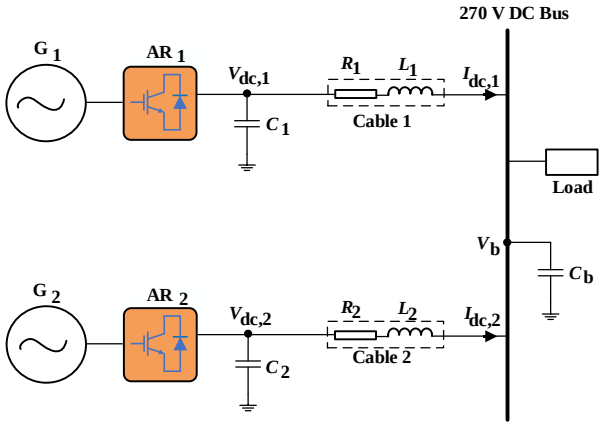

Fig. 4. Diagram of a two-source dc microgrid system.

Table I. Electrical power system parameters

Parameter	Symbol	Value
Main dc Bus rated voltage	V_{dc}^{*}	270 V
Local shunt capacitor	C_i	2.4 mF
Main dc bus capacitor	C_b	1.2 mF
Nominal droop gains	$k_{d,1}$	0.2353
	$k_{d,2}$	0.2353
Line resistance	R_1	0.003 Ω
	R_2	0.03 Ω
Line inductance	L_1	1 μH
	L_2	10 μH
Constant Power Load (CPL)	P_{CPL}	25 kW

Table II. Design space in Case Study I

Variable	Range	Step in sampling	Step in Optimization
k_{d1}	[0.2614, 0.2139]	0.0016	0.000056
k_{d2}	[0.2614, 0.2139]	0.0016	0.000056

proposed IAAI model is data-based, independent with the original system and the conventional approach. Therefore, the used ANN structure in IAAI method is flexible, can be totally different from that of conventional approach.

In Section V, the proposed IAAI method will be used to give a desired droop-coefficient design for the current sharing; further, in Section VI, an inversely designed ANN is trained to provide feasible injecting current references for the online converter control operation.

B. *Comparison with Inverse Function*

In mathematics, an inverse function is a function that "reverses" another function. Not all functions have inverse functions. Those that do are called invertible. For a function f: X → Y to have an inverse, it must have the property that for every y in Y, there is exactly one x in X such that f(x) = y. This property ensures that a function g: Y → X exists with the necessary relationship with f.

Regarding the original input/output relation as a function f: X → Y, then, both the IAAI model and inverse function can provide X with a given Y. However, there is no limit for training an IAAI model while inverse function does not always exist for f. In addition, if an inverse function exists, it should be theoretically and deterministically unique. Namely, given Y, only one X can be obtained. In contrast, as the AI model training starts from random values, the outputs of the trained IAAI model may vary after different training attempts.

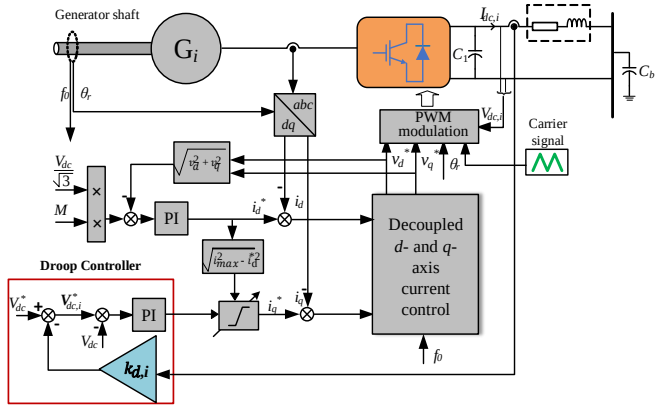

Fig. 5. Voltage-mode droop control scheme of a generator source fed by an active rectifier (AR) in the study islanded microgrid.

Therefore, the proposed IAAI model is much more flexible and easier to be generalized than the inverse function concept. The following contents will discuss three different cases of power converters. The conventional optimization-based design approach will be used in Case Study I (Section IV) while the proposed IAAI method will be applied to the other two cases.

IV. Case Study I – Optimization-Based Design for Current Sharing

In Sections IV & V, two different application methods of ANN will be discussed and compared. They are both used for the optimal droop coefficient design in a multi-source dc microgrid system. This section will start with a two-source islanded microgrid system using the optimization-based design method. The system diagram is shown in Fig. 4. G_1 and G_2 represent the two-generation sources for this microgrid. Each of them is feeding to an active rectifier (AR), which is parallel connected to the shared dc bus via a cable. This bus then supplies power to a simple linear load. Two ARs are controlled using the voltage-mode droop control scheme for current sharing between them. The following two subsections will first introduce the used droop control method and then discuss how to use the ANN-based optimization to choose the best control coefficients for this microgrid system.

A. *Analysis of the Conventional Droop Control Method*

The voltage-mode droop control scheme is shown in Fig. 5. The control structure is basically cascaded. It is made up of an inner loop for current control and outer loops for flux weakening and DC-link current control. The flux weakening control is employed to prevent the machine from operating above the base speed. The droop controller is responsible for the regulation of the DC-link current. The d and q axis reference current supplied to the current controller are generated from the flux-weakening and DC-link controller respectively, as shown in Fig. 5. Furthermore, vector control is employed to decouple the machine, thus, making it easy to independently control the torque and flux. A detailed analysis about the control structure

and design can be found in [24]. In this scheme, the measured branch output dc current $I_{dc,i}$ is used to generate the reference voltage $V^*_{dc,i}$, and this is expressed in (4):

$$V^*_{dc,i} = V^*_{dc} - k_{d,i} I_{dc,i} \tag{4}$$

where i =1,2 is the number of subsystems, V^*_{dc} is the rated dc bus voltage (270 V in this paper), $V^*_{dc,i}$ is the calculated reference voltage for each subsystem converter and $I_{dc,i}$ is the output current of each converter in the system, $k_{d,i}$ is the droop coefficient. The current sharing ratio among the two sources in steady-state is as expressed in (5), provided the effect of cable impedance on load sharing is ignored.

$$I_{dc,1} : I_{dc,2} = \frac{1}{k_{d,1}} : \frac{1}{k_{d,2}} \tag{5}$$

The droop coefficients $k_{d,i}$ of the converters are typically chosen to be proportional to the generators ratings to ensure an accurate current sharing, based on the assumption that the same nominal voltage V^*_{dc} is applied to each of the droop characteristics.

When the voltage drop on the cable (in Fig. 4) is put into consideration and the voltage control dynamics are ignored, the steady-state dc bus voltage can be expressed as in (6).

$$V_b = V^*_{dc,i} - I_{dc,i} R_i = V^*_{dc} - I_{dc,i}(k_{d,i} + R_i) \tag{6}$$

where V_b is the main dc voltage, R_i is the resistance of the individual cable connecting the ith source to the bus. Hence, the current sharing among the sources, assuming they are supplying together can be expressed as in (7).

$$I_{dc,1} : I_{dc,2} = \frac{1}{k_{d,1}+R_1} : \frac{1}{k_{d,2}+R_2} \tag{7}$$

Obviously, the cable resistance and droop gain will affect the power sharing ratio of the sources in steady states. By increasing the droop gain or cable resistance, the power output of the sources will be decreased. Furthermore, when the droop gain and cable resistance are similar, the accuracy of the power sharing among the sources will be degraded due to the existence of the cable resistance.

Generally, two approaches are commonly used in order to realize accurate load sharing. In the first approach, the droop coefficient is increased much higher than the cable resistance ($k_{d,i} \gg R_i$) such that the influence of the cable resistance on accurate load sharing becomes negligible. However, this will lead to poor voltage regulation and may affect the system's stability [25] and power quality [26]. Also, in low-voltage dc microgrids (for example power system on-board aircraft), the cable resistance cannot be simply ignored [25, 27]. This is because the line impedance in the low voltage dc microgrid is predominantly resistive.

In the second approach, the droop coefficient of the converters is compensated based on the estimated line resistance connecting the parallel-connected converters to the dc bus as can be found in [27]. This control method works in the same way as a virtual negative resistance to cancel the effect of the unequal cable resistance on accurate current sharing through compensation. However, the cable resistance is required for the compensation method, which is usually hard to obtain for real applications. The ANN-based optimization can provide an easy and effective way to get the optimal design of droop coefficients, as follows.

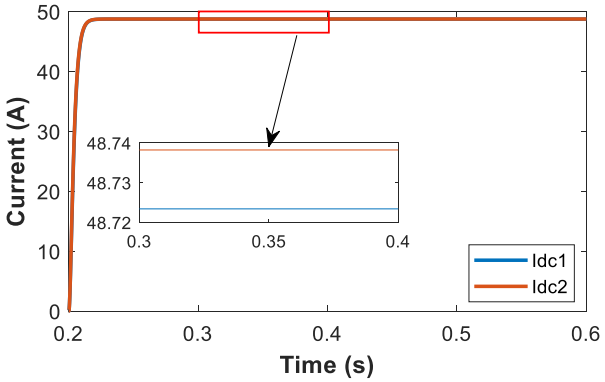

Fig. 6. Simulation results for the two-source microgrid case.

B. ANN-based optimization

Based on the optimization-based design approach (discussed in Section II.B), a neural network can be trained mapping from coefficients to the output dc currents, for this two-source current sharing problem. Therefore, the ANN represents the following relation:

$$y = F(x) \leftrightarrow (I_{dc,1}, I_{dc,2}) = F_1(k_{d,1}, k_{d,2}) \tag{8}$$

Based on the nominal value of $k_{d,i}$, a range can be pre-assumed for every droop coefficient for this optimization, for example, $\pm$10%. Then, to collect the ANN training data, the data points can be evenly sampled in this design space followed by getting the corresponding outputs ($I_{dc,i}$) via the detailed simulation. Using the training data, the desired ANN can be trained offline, i.e., updating the internal weights (ω) and bias (b) of ANN.

Therefore, following the original input-output relation in the system, the trained ANN can predict two output currents when given the combination of two droop coefficients. Since the ANN is very computationally light, after training, the exhaustive algorithm can be used for optimization. Namely, sample a large number of design points in the design space then generate all the output currents via ANN. Based on that, the optimal design, which has the minimum difference of the two output currents, can be quickly found.

C. Optimization results

Firstly, the detailed simulation model of the dc microgrid shown in Fig. 4 was developed in MATLAB Simulink. The electrical power system and line parameter used for the simulation are as shown in Table I.

The design space and the sampling step of the droop coefficient used for data generation and optimization is presented in Table II. Based on the sampling step for the data

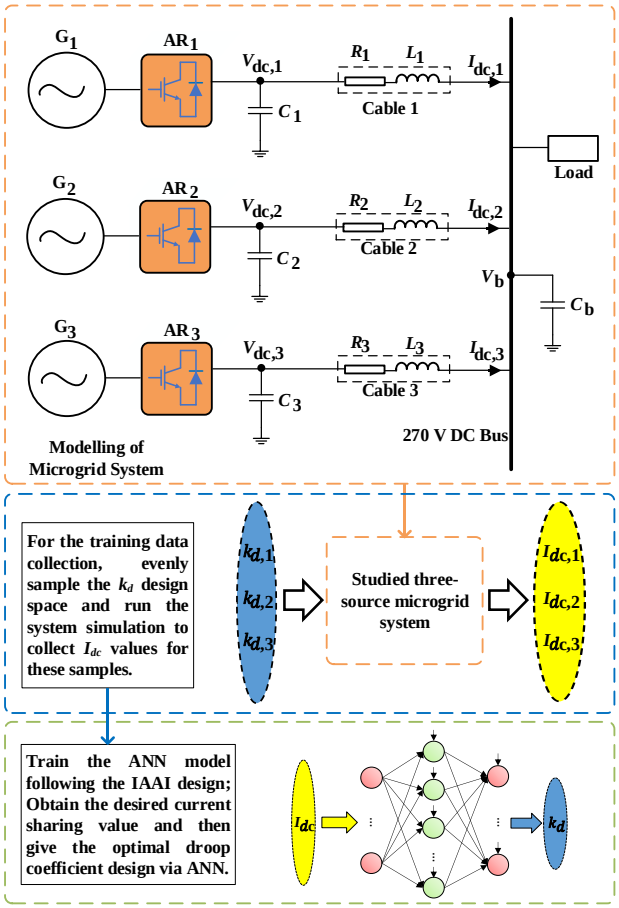

Fig. 7. Diagram of IAAI-based research thinking on three-source dc microgrid current sharing.

generation, a total of 961 combinations of the droop coefficient was used as input to the detailed simulation model. Hence, for every combination of the droop coefficient, the detailed simulation model is run in a loop and the output current of the converters are recorded.

The data generated is then used to train the ANN model. The ANN was trained using the *train* command in Matlab, which is a part of Deep Learning Toolbox [28]. The training performance was evaluated using the root mean square error (RMSE). The calculated RMSE was 0.025944 A and 0.021272 A for $I_{dc,1}$ and $I_{dc,2}$, respectively.

In the optimization stage, the trained ANN model was used to evaluate 724,201 (based on the sampling step shown in Table II) combinations of droop coefficients by predicting their corresponding output dc currents. Thereafter, the optimal droop coefficient combination that will yield the desired accurate current sharing between the converters was obtained as $k_{dc,1}^{opt}$=0.2459 and $k_{dc,1}^{opt}$=0.2189. The obtained optimal droop coefficients are then used in the detailed simulation model to evaluate the performance of the conventional droop control method. As shown in Fig. 6, the optimal droop coefficient can enhance the current sharing performance of the conventional droop control method, with $I_{dc,1}$ = 48.72 A and $I_{dc,2}$ = 48.74 A.

D. Discussion

Even though in this two-source microgrid case, the ANN-based optimization approach can provide a good droop coefficient design to achieve accurate current sharing without knowing the corresponding subsystem cable resistance, this optimization approach would become quite complicated for the cases with three or more sources. The reason is that the number of output currents will be 3+, which makes it difficult to set the two or more optimization objectives for the ideal current sharing. Regarding multi-objective optimization, it is a common sense that all the objectives should be integrated into one to determine the optimal design; However, the integrated function, as well as the weights of different objectives bring a new complexity to the optimization problem.

To address the above problems, the proposed IAAI can provide an excellent way to find the optimal droop coefficient design, because this IAAI method does not need an optimization process and is feasible for the microgrid case with an arbitrary number of sources, as below.

Table III. Additional parameters in Case Study II

Item	Value/Range
R_3	0.015 Ω
L_3	5 μH
Design range of $k_{d,i}$	[0.2614, 0.2139]
Sample step of $k_{d,i}$	0.0079

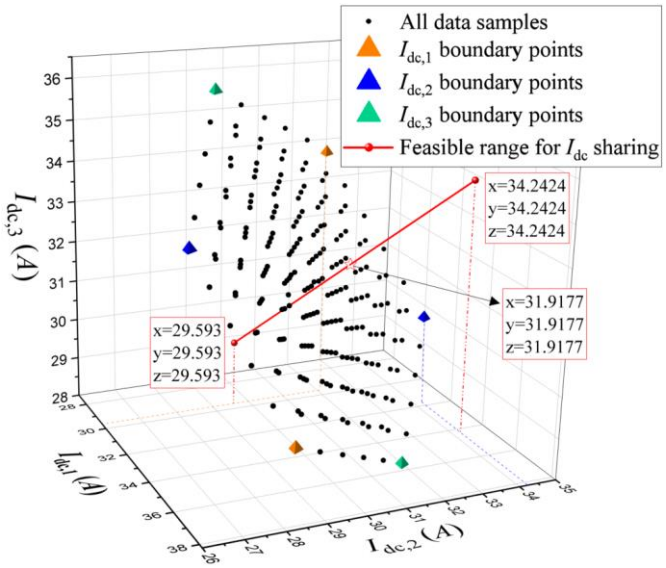

Fig. 8. Sample results in Case Study II and the feasible range for current sharing.

V. Case Study II – IAAI Method for Current Sharing

In this section, the proposed IAAI method will be employed to easily find the best design which can achieve accurate current sharing for a multi-source microgrid. Based on the two-source case in the last section, this section will elaborate on a three-source case using IAAI but note that the proposed method can be easily generalized for the system with four or more sources.

A. IAAI-based neural network design

As discussed in Section III, the IAAI method swops the original locations of inputs and outputs from the studied system to train the neural net. Therefore, in this three-source current-sharing case, the ANN will be designed to map from the output dc currents to the droop coefficients, as shown in Fig. 7. The

designed ANN represents the following relation:

$$y = F(x) \leftrightarrow \left(k_{d,1}, k_{d,2}, k_{d,3}\right) = F_2(I_{dc,1}, I_{dc,2}, I_{dc,3}) \quad (9)$$

Similar to the Case Study I, the collection process of training data can just be running the multiple simulations for the evenly distributed samples. After getting the coefficient sample data and the corresponding dc current data via simulations, they should be processed following (9) to train the desired ANN. After the ANN training, instead of using the exhaustive algorithm to do an optimization, an intersection-based approach will be employed to directly give the optimal coefficient design via the trained ANN, see below.

B. *Intersection-based approach*

In this three-source case, most of the parameters are the same as the above two-source case, including the nominal droop gains, $k_{d,i}$ design range, C_i, C_b, line impedance of two sources etc. The impedance values of the additional (3rd) line are given in Table III. Besides, the droop control scheme is also the same as in the above case.

In this section, the data distribution of the dc current samples will be analyzed to give a desired current-sharing value, which will then be feedforward to the trained ANN. The theoretical basis is that, in general, the shared current value should be just one desired value for all the output currents. Therefore, according to the collected 3-dimensional current data, an intersection can be generated as the feasible design range for the current sharing value. Any value out of this range would be unfeasible for current sharing in this specific system. After getting this intersection, the middle point will be chosen as the final desired current sharing value.

All the output current values of data samples are depicted in Fig. 8. Every black point clearly represents the I_{dc} distribution of one coefficient design point. In this three-source case, the ranges of $I_{dc,1}$, $I_{dc,2}$, and $I_{dc,3}$ are [29.593, 37.9642], [26.4919, 34.2424], and [28.1231, 36.2252], respectively. The boundary points are marked by triangles in Fig. 8. To generate a feasible range for every output current, first get the maximum value of three lower boundaries, which is 29.593 A (from $I_{dc,1}$, as shown by orange dotted lines in Fig. 8); Then, get the minimum value of three upper boundaries, which is 34.2424 A (from $I_{dc,2}$, as shown by blue dotted lines in Fig. 8). Based on these two values, the feasible design range (intersection) can be given as [29.593, 34.2424]. Since it is for the current sharing application, this feasible range is for all the output currents ($I_{dc,1}$, $I_{dc,2}$, and $I_{dc,3}$), not just for a specific one. Therefore, the corresponding 3-dimensional feasible range for the current sharing can be confirmed using this feasible range, which is demonstrated by a red solid line in Fig. 8. Finally, choose the middle point of this intersection (marked by a red star) as the final shared current value of all the three sources, which is 31.9177 A.

C. *IAAI design result and validation*

To train the proposed ANN in (9), samples were evenly collected in the 3D design space, where eleven values were sampled for each $k_{d,i}$. Therefore, the number of design points in the training data set is $11^3 = 1331$. For the ANN training, the *train* command in the Matlab Deep Learning Toolbox was again used. And the training performance (RMSE) for three k_d are all-around 0.001.

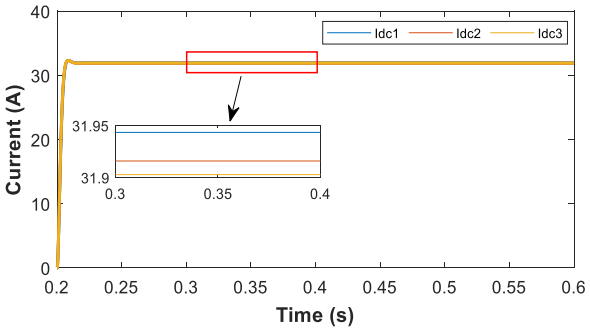

Fig. 9. Simulation results for the three-source microgrid case.

Then, using the combination of the desired sharing value, that is [31.9177; 31.9177; 31.9177], as the input of the trained IAAI-based ANN, the droop coefficient design can be quickly obtained (without an optimization): $k_{d,1} = 0.2335$, $k_{d,2} = 0.2067$, $k_{d,1} = 0.2218$.

Finally, to validate the obtained k_d design, they were input to the three-source microgrid system; after simulation, the obtained dc currents are $I_{dc,1} = 31.94$ A, $I_{dc,2} = 31.92$ A, $I_{dc,3} = 31.90$ A, as shown in Fig. 9. A good current sharing has been achieved.

D. *Discussion and Robustness Study*

Compared with Case Study I which uses the conventional optimization-based approach, in this Section, the IAAI approach provides an efficient way for the optimal droop coefficient design. After ANN training, the optimal design can be found based on just one I_{dc} design point, rather than doing an optimization using hundreds of points. In addition, the IAAI approach can be easily generalized to the microgrid case with 3+ sources while, for the optimization-based approach, it will be hard to balance the increasing number of objectives.

It is worth noting that, as discussed in [29], the intersection based approach can find almost the same optimal coefficients with the line droop compensator method (see [27]), which is based on the subsystem cable resistance. In contrast, the intersection-based approach just analyses the sample data distribution thus, it does not need to know the cable resistance beforehand, which is hard to estimate in a real microgrid system.

To further validate the proposed IAAI approach, a robustness study was undertaken based on changing the MG line resistance and inductance. Based on the above case, three different groups of parameters were considered: 1). A huge difference (doubled) in the system line resistances R_1 = 6 mΩ, R_2 = 60 mΩ, R_3 = 30 mΩ, and inductance of three cables stay unchanged; 2). Resistance of three cables is not changing but inductance are doubled, i.e., L_1 = 2 μH, L_2 20 μH, L_3 = 10μH; 3). A small difference in the system cable resistance, R_1=5 mΩ, R_2 = 34 mΩ, R_3= 10 mΩ, with inductance unchanged.

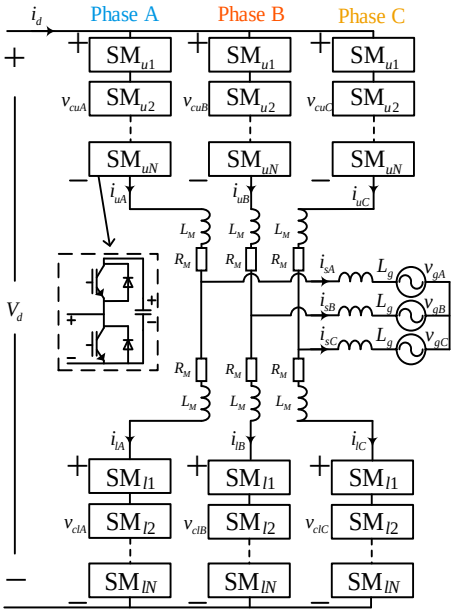

Fig. 10. MMC diagram.

Following the same IAAI approach, after setting each parameter group, 1331 data were newly collected to train new ANNs. Finally, the optimal k_d designs can be found via the trained ANNs when given the desired I_{dc} values (using the above intersection-based analysis).

The following optimal k_d are obtained for each of the case studies: 1). $k_{d,1}$ = 0.2174, $k_{d,2}$ = 0.1636, and $k_{d,3}$ = 0.1935; 2). $k_{d,1}$ = 0.2335, $k_{d,2}$ = 0.2065, and $k_{d,3}$ = 0.2215; 3). $k_{d,1}$ = 0.1558, $k_{d,2}$ = 0.1269, and $k_{d,3}$ = 0.1470.

Table IV. Robustness study by using IAAI

Parameter Group	$I_{dc,1}$ (A)	$I_{dc,2}$ (A)	$I_{dc,3}$ (A)	Desired I_{dc} (A)
1	31.88	31.85	31.87	31.87
2	31.92	31.92	31.92	31.92
3	31.38	31.35	32.13	31.57

As summarized by Table IV, the proposed IAAI method works very well for all these three situations. It can be observed from the results in the Group 1 that, despite the huge difference in the cable resistance, the proposed approach can still find the optimal k_d to yield desired current sharing. As shown in Group 2, the same current sharing and optimal droop coefficient is obtained even though the cable inductance is doubled, making the proposed method robust to the inductance changes.

E. *Stability issue*

The stability of this MG system can be verified by performing small signal stability around the MG steady-state operating point. Detailed comparative stability analysis of the droop control method and the impact of the droop coefficient have been carried out in [30]. To ensure a stable operation, the maximum value of $k_{d,i}$ can be given as: $\frac{V_{dc}^{*\,2}}{4P_{CPL}} - R_i$, where V_{dc}^* is the nominal dc voltage, P_{CPL} is the CPL power, and R_i is the cable resistance. Therefore, for the MG parameters (Table I) used in this paper and for the training data extraction, the maximum droop coefficient is 0.699. As shown in Tables II&III, the design ranges of $k_{d,i}$ used in this paper are all much smaller than this max limit. Thus, it can be concluded that the IAAI-based $k_{d,i}$ design is well within the acceptable design range for a stable operation.

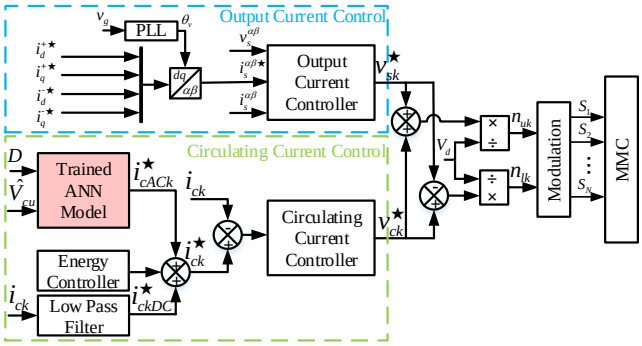

Fig. 11. The control block diagram of proposed MMC.

VI. Case Study III

A. *Motivation of this case study*

The modular multilevel converter (MMC) is a promising topology for converter-based high voltage direct current (HVDC) systems because of the following pros: lower harmonics, modularity, scalability, and few harmonic filter requirements [31]. However, the ripples of the capacitor voltage in MMC will be enlarged if under unbalanced grid fault conditions. Since high capacitor voltage ripples deteriorate their lifetimes and may even cause the tripping problem, it is essential to regulate the ripples. To do that, it is a common way of injecting the circulating currents with a double fundamental frequency. However, finding a proper circulating current reference under various unbalanced grids to achieve desired ripples analytically is very complicated [32-34]. The analytical frequency-domain methods [32, 34] for reducing the ripples require strong control expertise, which makes them difficult to reproduce or understood by practicing engineers in other fields. In contrast, the proposed ANN does not require any control or frequency-domain derivation, an easier approach.

In this section, the proposed IAAI method will be used to train an ANN, which acts as a dedicated surrogate model to provide a proper circulating current reference for the control of an MMC under unbalanced grid faults. In that way, the MMC operating region can be effectively extended. After training, the designed ANN model will be applied to simulations and an experiment rig for the validation, providing the desired circulating current reference to reduce the capacitor voltage.

In the following subsections, the MMC operation principle and control will be first introduced. After that, the purpose of using ANN and the ANN design details will be given. Then, the validation results from both simulation and experiment will be presented. Finally, the MMC stability issue is discussed.

B. *MMC topology and control*

Fig. 10 shows the topology of a half-bridge submodule MMC. It is a three-phase grid-connected MMC, where each phase has two arms: upper and lower arm. Each arm is comprised of N series-connected half bridge submodules, and an arm inductor (L_M) [35]. The submodule (SM) capacitor voltage is kept close

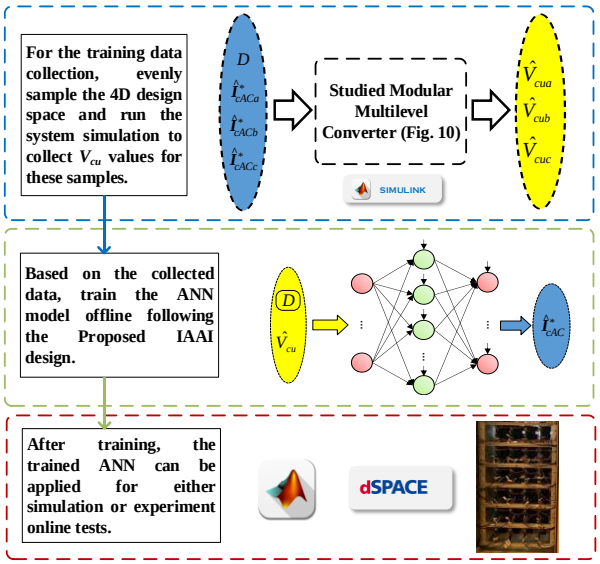

Fig. 12. Diagram of the ANN aided MMC operating region extension.

to the rated dc voltage by the MMC controller. In this way, the single submodule can be controlled as a voltage source by inserting or bypassing the submodules. The MMC output ac voltage can be controlled by changing the number of inserted submodules [36, 37].

The directions of the upper arm current (i_{uk}) and lower arm current (i_{lk}) are shown in Fig. 10, k denotes the ac phase. By applying Kirchhoff's voltage law to the MMC circuit, the MMC dynamic equations can be derived as follows:

$$\frac{V_d(t)}{2} - v_{cuk}(t) - R_m i_{uk}(t) - L_M \frac{di_{uk}(t)}{dt} = v_{gk}(t) + L_g \frac{di_{sk}(t)}{dt} \quad (10)$$

$$\frac{V_d(t)}{2} - v_{clk}(t) - R_m i_{lk}(t) - L_M \frac{di_{lk}(t)}{dt} = -v_{gk}(t) - L_g \frac{di_{sk}(t)}{dt} \quad (11)$$

where V_d is dc link voltage, i_d is the dc current. v_{cuk} and v_{clk} are the upper and lower arm voltage in phase k respectively, i_{uk} and i_{lk} are the upper and lower arm current in phase k respectively. k=0, 1, 2 (0 for phase A, 1 and 2 for B and C respectively). v_{gk} is the ac voltage from the grid side. L_g is the output inductance and i_{sk} is output current.

The output current i_{sk} and circulating current i_{ck} can be defined as below:

$$i_{sk}(t) = i_{uk}(t) - i_{lk}(t) \quad (12)$$

$$i_{ck}(t) = \frac{1}{2}[i_{uk}(t) + i_{uk}(t)] = I_{ckDC} + \hat{I}^*_{cACk}\cos(2\omega t + \theta_{vk-}) \quad (13)$$

I_{ckDC} is the dc component of circulating current, $\hat{I}^*_{cACk}\cos(2\omega t + \theta_{vk-})$ is ac component of three-phase circulating current, ω is the fundamental angular frequency, and $\theta_{vk-}$is the phase angle of negative-sequence voltage. The injected ac circulating currents are double fundamental frequency, negative-sequence phases [0, -4/3π, -2/3π] with different amplitudes ($\hat{I}_{cACa}$,$\hat{I}_{cACb}$,$\hat{I}_{cACc}$).

The dynamic equations of the output ac current and circulating current (i_c) can be derived from (10)-(13):

$$\frac{di_{sk}(t)}{dt} = \frac{1}{L_M+2L_g}[v_{clk}(t) - v_{cuk}(t) - 2v_{gk}(t)] \quad (14)$$

Table V. Vector definition of different unbalanced grid conditions

Fault Types	Vector Definitions
Two-phase-to-ground fault	$\hat{V}_{ga\_pu}=1$, $\hat{V}_{gb\_pu}=-\frac{1}{2}D-j\frac{\sqrt{3}}{2}D$, $\hat{V}_{gc\_pu}=-\frac{1}{2}D+j\frac{\sqrt{3}}{2}D$
Three-phase-to-ground fault	$\hat{V}_{ga\_pu}=D$, $\hat{V}_{gb\_pu}=-\frac{1}{2}D-j\frac{\sqrt{3}}{2}D$, $\hat{V}_{gc\_pu}=-\frac{1}{2}D+j\frac{\sqrt{3}}{2}D$
Phase-to-phase short-circuit fault	$\hat{V}_{ga\_pu}=1$, $\hat{V}_{gb\_pu}=-\frac{1}{2}-j\frac{\sqrt{3}}{2}D$, $\hat{V}_{gc\_pu}=-\frac{1}{2}+j\frac{\sqrt{3}}{2}D$
Single-phase-to-ground fault	$\hat{V}_{ga\_pu}=D$, $\hat{V}_{gb\_pu}=-\frac{1}{2}-j\frac{\sqrt{3}}{2}$, $\hat{V}_{gc\_pu}=-\frac{1}{2}+j\frac{\sqrt{3}}{2}$

Table VI. MMC parameters in simulation and experiment

	Simulation	Experiment
Number of SMs per arm (N)	100	4
Rated dc voltage (V_d)	200 kV	200 V
Rated active power	150 MW	1 kW
Nominal SM capacitance (C)	3.75 mF	2000 μF
Nominal SM capacitor voltage (V_c)	2 kV	50 V
Rated frequency (f)	50 Hz	50 Hz
Arm inductance (L_m)	50.9 mH	10 mH
Sample frequency	10 kHz	10 kHz
Grid voltage magnitude	100 kV	83 V
Dip severity grid factor (D)	0.7	0.5

$$\frac{di_{ck}(t)}{dt} = \frac{1}{2L_M}[v_d(t) - v_{clk}(t) - v_{cuk}(t)] \quad (15)$$

Based on equations (14) and (15), the output current and circulating current can be controlled.

The control block diagram of the proposed method is shown in Fig. 11. The MMC controller comprises of two main parts. (1). Output Current Controller: proportional resonant (PR) controller is used in the output controller to control the output current of the MMC in grid-connected operation. This controller is conventional, and more details can be found in [36]; (2). Proposed ANN and circulating current controller: When an unbalanced grid fault happens, the proposed ANN model will generate three-phase circulating current references based on desired capacitor voltages $\hat{V}_{cu}$, detected grid voltage dip factor D, and the grid fault type. Then, the circulating current controller enables the MMC to track its circulating current references. In this paper, the PR controller is used to track the ac circulating current [36]. The proposed ripple reduction method reduces the SM voltage ripple by injecting ac circulating current under unbalanced grid conditions. The energy controller ensures that the total amount of energy stored inside the converter is always controllable to stabilize the MMC

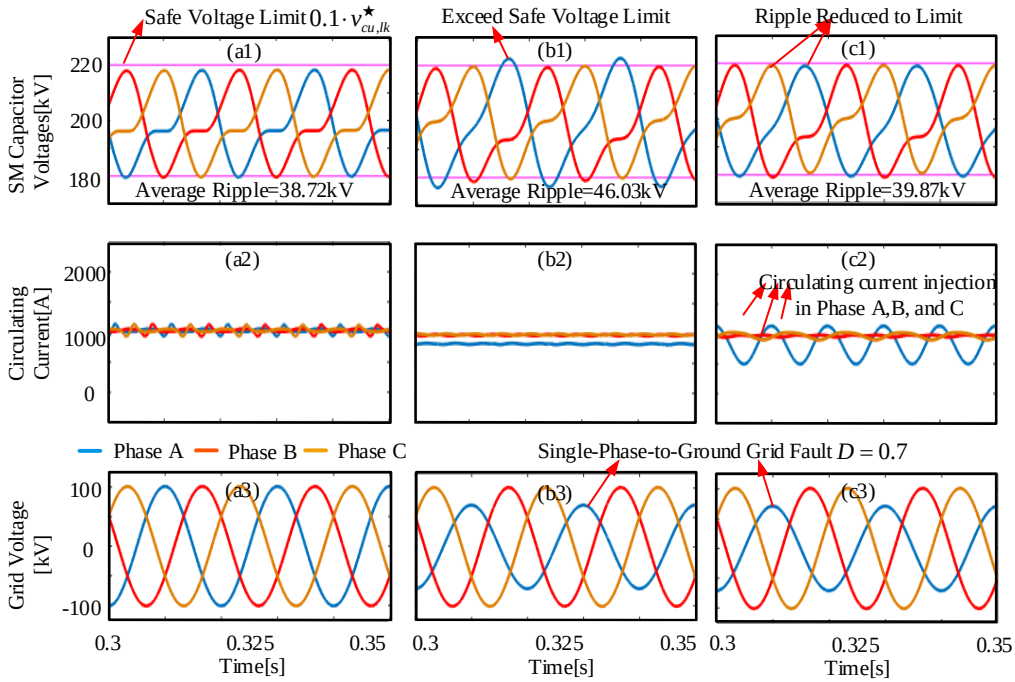

Fig. 13. Simulation results: (a) normal grid condition; (b) single-phase-to-ground grid without proposed method; (c) single-phase-to-ground grid with proposed method.

system under unbalanced grid conditions. The detailed information about these two energy controllers can be found in [36] and [38].

C. Unbalanced grid condition and the ANN deployment

The proposed reference surrogate model is constructed by using a 3-layer ANN. The number of hidden-layer neuron can be set as an algorithm developer but in this case, it is simply fixed as 9 because the designed ANN can be easily trained and the resulting model can give a good test performance. As shown in Fig. 12, there are four design variables in this case, where $\hat{I}^{*}_{cACa}, \hat{I}^{*}_{cACb}, \hat{I}^{*}_{cACc}$ are circulating current peak value references and D is grid dip severity factor. The severity of two-phase-to-ground grid fault depends on D. The range of D is [0,1], where 1 means normal grid, and 0 means short circuit, more practices about D can be found in [39, 40].

The proposed method can also easily be extended to any unbalanced grid condition. There are 4 types of unbalanced grid conditions [39, 40]: Two-phase-to-ground fault, three-phase-to-ground fault, single-phase-to-ground fault, and phase-to-phase short circuit fault. The vector definitions of other unbalanced grid conditions are shown in Table V. By the type of unbalanced grid condition and changing D from [0, 1], we can cover all possible fault scenarios by doing numerous parallel simulations and extracting corresponding data. This process can be significantly accelerated by paralleling the tasks using a computer cluster that contains many CPU cores. Therefore, the only limitation to extend our method to any other fault condition is computational capacity. If we have enough computational power, the data for other unbalanced fault conditions can be quickly collected. Then, new ANNs can be trained by the collected data and the circulating current reference for different unbalanced grid conditions can be calculated easily. The specifications of studied simulation and experiment systems are given in Table VI.

After the data collection, following the IAAI design, the proposed ANN surrogate represents the relationship mapping from the capacitor voltage and D to the desired circulating current amplitude/reference:

$$y = F(x) \Leftrightarrow (\hat{I}^{*}_{cACa}, \hat{I}^{*}_{cACb}, \hat{I}^{*}_{cACc}) = F_3(D, \hat{V}_{cua}, \hat{V}_{cub}, \hat{V}_{cuc}) \quad (16)$$

which is shown in Fig. 12. $\hat{V}_{cua}, \hat{V}_{cub}, \hat{V}_{cuc}$ mean the peak value of capacitor voltage ripple in Phase A, B and C respectively.

It is noted that the grid dip severity factor D is not located in the ANN outputs, which is mainly because the aim of ANN design here is to provide the circulating current reference, rather than predicting the grid dip severity condition. Another important reason of regarding D as an ANN input is that D is a crucial parameter for the unbalanced grid fault condition, which should be an essential information for the ANN. Therefore, this ANN design represents a feasible variant of IAAI method: the ANN inputs and outputs are not necessarily swopped for all the elements, some important elements may stay in the ANN inputs, which can feedforward important (even essential) information to the desired ANN.

D. Data collection and ANN training

The feedback of the designed ANN is triggered when the unbalanced grid detector detects an unbalanced grid fault. After training, the ANN can give feasible circulating current references (i^{*}_{cACk}) to control the SM capacitor voltages in a desired way. This case takes two-phase-to-ground grid fault as an example. The vector definition of the two-phase-to-ground grid fault can be described based on [40] as:

$$\hat{V}_{ga\_pu} = 1, \hat{V}_{gb\_pu} = -\frac{1}{2}D - j\frac{\sqrt{3}}{2}D, \hat{V}_{gc\_pu} = -\frac{1}{2}D + j\frac{\sqrt{3}}{2}D \quad (17)$$

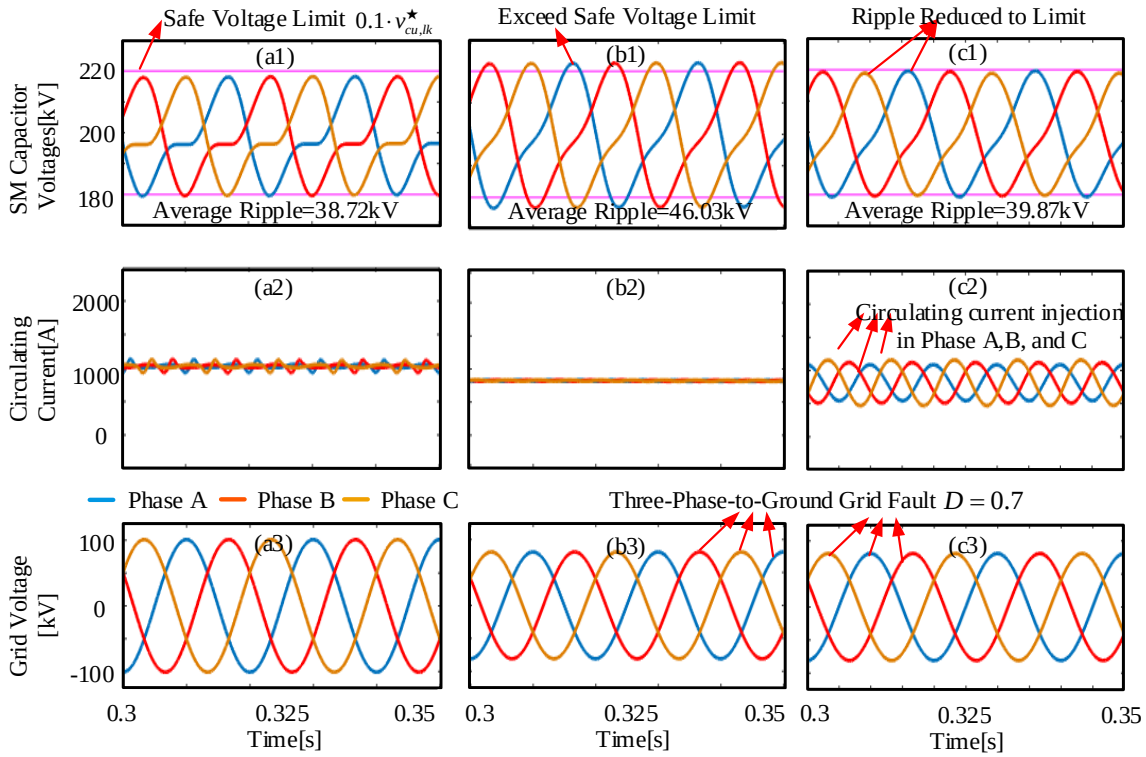

Fig. 14. Simulation results: (a) normal grid condition; (b) three-phase-to-ground grid without proposed method; (c) three-phase-to-ground grid with proposed method.

where $\hat{V}_{ga\_pu}, \hat{V}_{gb\_pu}, \hat{V}_{gc\_pu}$ are per unit values of the grid voltages in Phases A, B, and C.

Circulating current circulates inside the MMC without affecting the ac output currents. It only influences the internal performance of the MMC system. The circulating currents are defined as a parameter containing both dc and ac components as (13).

Regarding the training data generation, they can be extracted either from a detailed simulation or from an experimental setup. In this work, the data were collected from simulations, then the method was validated in both a high voltage simulation model and a low voltage experimental setup. In the high voltage simulation cases, the sweep values of input data are: grid dip severity D = [0.5, 0.6, 0.7, 0.8, 0.9]; three circulating currents $\hat{I}^{*}_{cACa,b,c}$ = [0, 50, 100, 150, 250, 300, 350, 400] for three phases *a*, *b*, *c*; the output data are three capacitor voltages $\hat{V}_{cua,b,c}$. The total number of data points is hence $5 \times 8 \times 8 \times 8 = 2560$. In the simulation model that resembles the experimental setup, the sweep values of input data are: D = [0.5, 0.6, 0.7, 0.8, 0.9], $\hat{I}^{*}_{cACa,b,c}$ = [0.3, 0.5, 0.7, 0.9, 1.1, 1.3, 1.5]. Therefore, the total number of data points is $5 \times 7 \times 7 \times 7$=1715. The output data $\hat{V}_{cua,b,c}$ can be then collected after each time of running the model. The paralleled simulations helped us to accelerate the simulation process. In particular, a workstation with a 24-core CPU was utilized for the data collection. The overall data collection time was approximately 14 *mins* for 2560 samples and was approximately 10 *mins* for 1715 data.

Based on the collected data, the ANNs were also trained using the *train* command in Matlab. For the training parameters, the learning rate is set as 0.1, the training goal (RMSE) is set as 0.001, and the maximum epoch number is 500. The designed ANN can be trained in a few seconds on a standard computer. Since the training starts from random values, the training was tried 10 times and the best one is picked for the following online validation.

E. Simulation results

After training, the ANN model was finally used to calculate the injected circulating current references for the MMC system under grid faults. The inputs of the ANN model are the grid dip severity factor D and safe SM capacitor voltage limit, then the outputs of the ANN are the three-phase circulating current references. In this section, the trained ANN model was compiled in the SIMULINK model. The simulation results of single-phase-to-ground and three-phase-to-ground are shown in Figs. 13 and 14, respectively.

Obviously, three-phase capacitor voltages are balanced under a balanced grid. In addition, the voltage is within the safe limit, as shown in Figs. 13 and 14 (a1). The average ripple (peak to peak value of capacitor voltage) is 38.72 kV, and the unbalanced degree (UD) is 0.046%. Unbalanced degree (UD) is defined in (18) as:

$$UD = [max(\hat{V}_{cua}, \hat{V}_{cub}, \hat{V}_{cuc}) - min(\hat{V}_{cua}, \hat{V}_{cub}, \hat{V}_{cuc})]/V_{avg} \times 100\% \quad (18)$$

where $\hat{V}_{cua,b,c}$ is SM capacitor voltage peak value in phase A, B, and C, respectively. V_{avg} is the average voltage of three phase capacitor voltages.

The capacitor voltages become unbalanced under single-phase-to-ground and three-phase-to-ground fault conditions, as shown in Figs. 13 and 14 (b1). In those figures, only the upper arm SM capacitor voltages are shown because the upper and

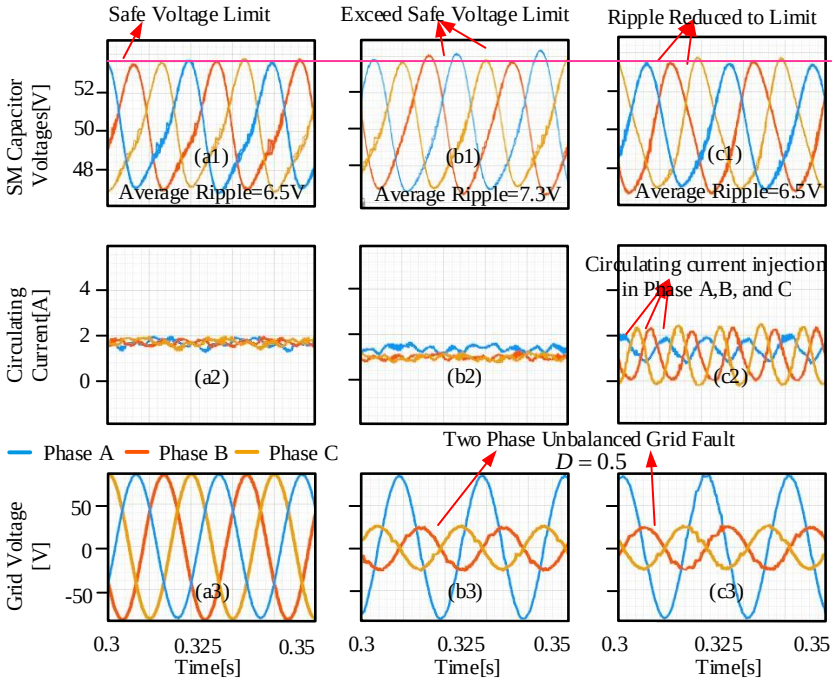

Fig. 15. Experimental results: (a) Normal grid condition. (b) Unbalanced grid condition without proposed method. (c) Unbalanced grid condition with the proposed method.

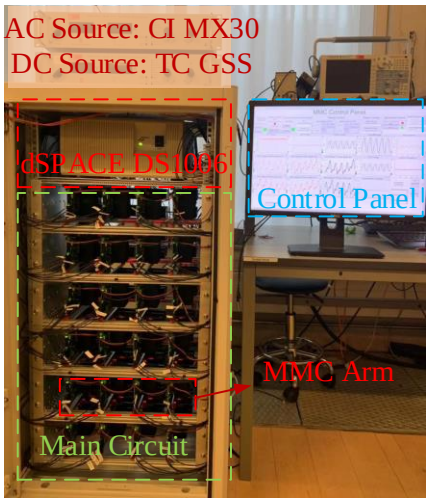

Fig. 16. MMC setup.

lower arm are symmetrical. And also, the capacitor voltage balancing algorithm is applied in modulation as shown in Fig. 11, then the SM capacitors in one arm are identical; Thus 4 capacitor voltages in one arm look like only one voltage. Moreover, the capacitor voltage amplitudes exceed the limit, which are shown in Figs. 13 and 14 (b1). The average ripple increases to 46.03 kV in both fault conditions. The *UD* increases to 1.51%.

The capacitor voltages can be effectively reduced to a safe voltage limit by the proposed IAAI method, as tested in the simulations. As shown in Fig. 13(c2), under the single-phase-to-ground condition, the amplitudes of injected ac circulating current components are $\hat{I}_{cACa} = 391.8\ A$, $\hat{I}_{cACb} = 60.56\ A$, and $\hat{I}_{cACc} = 60.67\ A$, respectively. For the three-phase-to-ground condition in Fig. 14(c2), $\hat{I}_{cACa} = 276.2\ A$, $\hat{I}_{cACb} = 324.3\ A$, and $\hat{I}_{cACc} = 387.5\ A$. As a result, the average ripple turns to be 39.87 kV in both fault conditions, and the *UD* is both reduced to 0.59%. With the proposed method, MMC capacitor overvoltage trip can be prevented when *D*=0.7.

F. Experimental results

In the experimental rig, the trained ANN model was finally used to calculate the injected circulating current references for the MMC system under two-phase-to-ground grid faults. The same with above simulation cases, the inputs of the ANN model are the grid dip severity factor *D* and safe SM capacitor voltage limit, then the outputs of the ANN are the three-phase circulating current references. The trained ANN model was compiled in the SIMULINK model. This model can both be applied in the PLECS Blockset software (for offline simulation) and the dSPACE DS1006 platform (for real-time control).

In this study, the experiment is carried out in a scaled-down three-phase grid-connected MMC setup with 4 half-bridge SMs per arm. The MMC controller is implemented in DS1006 from dSPACE. The specifications of the experimental setup are listed in Table VI. Note that, the value of arm resistance and grid inductance are usually very small thus ignored here. As mentioned, the data points for experiments were collected from a detailed simulation model using the same parameters with the lab setup. In this way, the data extraction time was greatly saved. Test results are given in Fig. 15 and the photo of MMC experimental setup is shown in Fig. 16.

Obviously, three-phase capacitor voltages are balanced under a balanced grid. In addition, the voltage is within the safe limit, as shown in Fig. 15(a1). The average ripple is 6.5 V, and the UD is 0.18%. Similar with the above simulation results, the capacitor voltages become unbalanced under two-phase-to-ground faults, as shown in Fig. 15(a1), (b1), (c1). The capacitor voltage amplitudes exceed the limit under the fault condition, which is shown in Fig. 15(b1). The average ripple increases to 7.3 V. The *UD* increases to 1.112%.

The proposed method can effectively reduce the capacitor voltages to a safe voltage limit in the experiment as shown in Fig. 15(c1). The amplitudes of injected ac circulating current components are $\hat{I}_{cACa} = 0.51\ A$, $\hat{I}_{cACb} = 1.13\ A$, and $\hat{I}_{cACc} = 1.29\ A$, respectively. The average ripple here is 6.5 V, and the *UD* is reduced to 0.5%. With the proposed method, MMC capacitor overvoltage trip can be prevented when *D*=0.5.

G. Stability issue

The MMC controller structure of this paper is widely used in many applications such as HVDC and medium voltage DC network. The stability issue has been well researched by many papers [41, 42]. The only difference is that, in our case, the circulating current reference $\hat{I}^*_{cAC}$ is given by the proposed ANN. To ensure the stability of the system, the $\hat{I}^*_{cAC}$ max limit should be applied. This limit is determined by the IGBT current rating of MMC [41]. As shown in above ANN part, the $\hat{I}^*_{cAC}$

range for data collection is [0, 400] A for simulation and [0.3, 1.5] A for the experiment, which are well selected for specific systems. What is more, the same $\hat{I}_{cAC}^{*}$ max limit is also applied during the real-time operations, which can prevent any possible large references given by ANN. Based on that, the system stability is ensured.

VII. Conclusion

This paper proposes a novel concept for the AI application, which swops the locations of original inputs and outputs for the AI model training (named as Inverse Application of Artificial Intelligence, IAAI). Compared to the conventional optimization-based method, the proposed IAAI method can achieve a fast coefficient/reference selection for the control of power converters, without an optimization process.

In the case study, two different control cases are given to show the validation of this method. One is for the droop coefficient design which aims at the current sharing in a microgrid, the other is for the operating region extension of MMC under unbalanced grid faults. Both AI models can achieve the desired performance based on the proposed inverse application concept. It is found that, compared with the conventional methods, the IAAI method turns out to be simple and efficient because there is no need for an extra optimization process or substantial derivations in this data-driven model-free approach.

The proposed ANN IA method is model-free and data-based, which does not require the model analysis or derivations. However, it is worth noting that, before collecting data, the design space as well as the operation region of the studied problem should be well confirmed. The inputs/outputs of ANN usually need a selection process. Moreover, if the topic to be addressed is super large, a possible way is dividing it into several sub-topics, by using ML classification techniques.

Reference

[1] R. S. Sutton and A. G. Barto, *Reinforcement learning: An introduction*. MIT press, 2018.

[2] S. Skansi, *Introduction to Deep Learning: from logical calculus to artificial intelligence*. Springer, 2018.

[3] S. Zhao, F. Blaabjerg, and H. Wang, "An overview of artificial intelligence applications for power electronics," *IEEE Transactions on Power Electronics*, 2020.

[4] S. Vazquez *et al.*, "An Artificial Intelligence Approach for Real-Time Tuning of Weighting Factors in FCS-MPC for Power Converters," *IEEE Transactions on Industrial Electronics*, 2021.

[5] T. Guillod, P. Papamanolis, and J. W. Kolar, "Artificial neural network (ANN) based fast and accurate inductor modeling and design," *IEEE Open Journal of Power Electronics*, vol. 1, pp. 284-299, 2020.

[6] Y. Gao, T. Yang, S. Bozhko, P. Wheeler, and T. Dragičević, "Filter Design and Optimization of Electromechanical Actuation Systems Using Search and Surrogate Algorithms for More-Electric Aircraft Applications," *IEEE Transactions on Transportation Electrification*, vol. 6, no. 4, pp. 1434-1447, 2020.

[7] O. Dahhani, I. Boumhidi, J. Tekobon, and C. Nichita, "Wind power system control based on least square support vector machines algorithms," in *2016 IEEE 16th International Conference on Environment and Electrical Engineering (EEEIC)*, 2016: IEEE, pp. 1-5.

[8] C. Seijas, A. Caralli, S. Villazana, and E. Carpentiero, "Active Input Line Current Shaping using Support Vector Machines," in *2006 International Caribbean Conference on Devices, Circuits and Systems*, 2006: IEEE, pp. 227-231.

[9] A. Lidozzi, L. Solero, F. Crescimbini, and A. Di Napoli, "SVM PMSM drive with low resolution Hall-effect sensors," *IEEE Transactions on Power Electronics*, vol. 22, no. 1, pp. 282-290, 2007.

[10] M. Novak and T. Dragicevic, "Supervised Imitation Learning of Finite-Set Model Predictive Control Systems for Power Electronics," *IEEE Transactions on Industrial Electronics*, vol. 68, no. 2, pp. 1717-1723, 2020.

[11] S. Wang, T. Dragicevic, Y. Gao, and R. Teodorescu, "Neural Network based Model Predictive Controllers for Modular Multilevel Converters," *IEEE Transactions on Energy Conversion*, 2020.

[12] T. Dragičević, P. Wheeler, and F. Blaabjerg, "Artificial intelligence aided automated design for reliability of power electronic systems," *IEEE Transactions on Power Electronics*, vol. 34, no. 8, pp. 7161-7171, 2018.

[13] K. Hornik, M. Stinchcombe, and H. White, "Multilayer feedforward networks are universal approximators," *Neural networks*, vol. 2, no. 5, pp. 359-366, 1989.

[14] T. Dragicevic, S. Vazquez, and P. Wheeler, "Advanced control methods for power converters in dg systems and microgrids," *IEEE Transactions on Industrial Electronics*, 2020.

[15] Q. Xu, T. Dragicevic, L. Xie, and F. Blaabjerg, "Artificial Intelligence based Control Design for Reliable Virtual Synchronous Generators," *IEEE Transactions on Power Electronics*, 2021.

[16] I. S. Mohamed, S. Rovetta, T. D. Do, T. Dragicević, and A. A. Z. Diab, "A neural-network-based model predictive control of three-phase inverter with an output $ LC $ filter," *IEEE Access*, vol. 7, pp. 124737-124749, 2019.

[17] S. Wang, T. Dragicevic, G. F. Gontijo, S. K. Chaudhary, and R. Teodorescu, "Machine Learning Emulation of Model Predictive Control for Modular Multilevel Converters," *IEEE Transactions on Industrial Electronics*, 2020.

[18] D. Wang *et al.*, "Model predictive control using artificial neural network for power converters," *IEEE Transactions on Industrial Electronics*, vol. 69, no. 4, pp. 3689-3699, 2021.

[19] A. N. Akpolat *et al.*, "Dynamic stabilization of dc microgrids using ann-based model predictive control," *IEEE Transactions on Energy Conversion*, vol. 37, no. 2, pp. 999-1010, 2021.

[20] Z. Li, Y. Gao, X. Zhang, B. Wang, and H. Ma, "A Model-Data-Hybrid-Driven Diagnosis Method for Open-Switch Faults in Power Converters," *IEEE Transactions on Power Electronics*, 2020.

[21] S. D. Sudhoff, *Power magnetic devices: a multi-objective design approach*. John Wiley & Sons, 2014.

[22] Y. Gao, T. Yang, X. Wang, S. Bozhko, and P. Wheeler, "Machine Learning Based Correction Model in PMSM Power Loss Estimation for More-Electric Aircraft Applications," in *2020 23rd International Conference on Electrical Machines and Systems (ICEMS)*, 2020: IEEE, pp. 1940-1944.

[23] Y. Gao, T. Yang, S. Bozhko, P. Wheeler, T. Dragicevic, and C. Gerada, "Neural Network aided PMSM multi-objective design and optimization for more-electric aircraft applications," *Chinese Journal of Aeronautics*, 2021.

[24] S. Bozhko, S. S. Yeoh, F. Gao, and C. Hill, "Aircraft starter-generator system based on permanent-magnet machine fed by active front-end rectifier," in *IECON 2014-40th Annual Conference of the IEEE Industrial Electronics Society*, 2014: IEEE, pp. 2958-2964.

[25] N. Yang, D. Paire, F. Gao, A. Miraoui, and W. Liu, "Compensation of droop control using common load condition in DC microgrids to improve voltage regulation and load sharing," *International Journal of Electrical Power & Energy Systems*, vol. 64, pp. 752-760, 2015.

[26] F. Gao, S. Bozhko, G. Asher, P. Wheeler, and C. Patel, "An improved voltage compensation approach in a droop-controlled DC power system for the more electric aircraft," *IEEE Transactions on Power Electronics*, vol. 31, no. 10, pp. 7369-7383, 2015.

[27] A. Tah and D. Das, "An enhanced droop control method for accurate load sharing and voltage improvement of isolated and interconnected DC microgrids," *IEEE Transactions on Sustainable Energy*, vol. 7, no. 3, pp. 1194-1204, 2016.

[28] MathWorks. "Support Documentation, trainbr (R2020a)." MathWorks. https://uk.mathworks.com/help/deeplearning/ref/trainbr.html (accessed.

[29] H. Hussaini, T. Yang, Y. Gao, C. Wang, T. Dragicevic, and S. Bozhko, "Droop Coefficient Design in Droop Control of Power Converters for Improved Load Sharing: An Artificial Neural Network Approach," in *2021 IEEE 30th International Symposium on Industrial Electronics (ISIE)*, 2021: IEEE, pp. 1-6.

[30] F. Gao *et al.*, "Comparative stability analysis of droop control approaches in voltage-source-converter-based DC microgrids," *IEEE Transactions on Power Electronics*, vol. 32, no. 3, pp. 2395-2415, 2016.

[31] A. Lesnicar and R. Marquardt, "An innovative modular multilevel converter topology suitable for a wide power range," in *2003 IEEE Bologna Power Tech Conference Proceedings*, 2003, vol. 3: IEEE, p. 6 pp. Vol. 3.

[32] H. Kim, S. Kim, Y.-H. Chung, D.-W. Yoo, C.-K. Kim, and K. Hur, "Operating region of modular multilevel converter for HVDC with controlled second-order harmonic circulating current: Elaborating PQ capability," *IEEE Transactions on Power Delivery*, vol. 31, no. 2, pp. 493-502, 2015.

[33] E. Rodriguez *et al.*, "Closed-loop analytic filtering scheme of capacitor voltage ripple in multilevel cascaded H-bridge converters," *IEEE Transactions on Power Electronics*, vol. 35, no. 8, pp. 8819-8832, 2020.

[34] J. Pou, S. Ceballos, G. Konstantinou, V. G. Agelidis, R. Picas, and J. Zaragoza, "Circulating current injection methods based on instantaneous information for the modular multilevel converter," *IEEE Transactions on Industrial Electronics*, vol. 62, no. 2, pp. 777-788, 2014.

[35] K. Ilves, S. Norrga, L. Harnefors, and H.-P. Nee, "On energy storage requirements in modular multilevel converters," *IEEE transactions on power electronics*, vol. 29, no. 1, pp. 77-88, 2013.

[36] K. Sharifabadi, L. Harnefors, H.-P. Nee, S. Norrga, and R. Teodorescu, *Design, control, and application of modular multilevel converters for HVDC transmission systems*. John Wiley & Sons, 2016.

[37] J. I. Leon, S. Vazquez, and L. G. Franquelo, "Multilevel converters: Control and modulation techniques for their operation and industrial applications," *Proceedings of the IEEE*, vol. 105, no. 11, pp. 2066-2081, 2017.

[38] A. Antonopoulos, L. Ängquist, L. Harnefors, K. Ilves, and H.-P. Nee, "Global asymptotic stability of modular multilevel converters," *IEEE Transactions on Industrial Electronics*, vol. 61, no. 2, pp. 603-612, 2013.

[39] T. Tanaka, K. Ma, H. Wang, and F. Blaabjerg, "Asymmetrical reactive power capability of modular multilevel cascade converter based STATCOMs for offshore wind farm," *IEEE Transactions on Power Electronics*, vol. 34, no. 6, pp. 5147-5164, 2018.

[40] M. H. Bollen, "Understanding power quality problems," in *Voltage sags and Interruptions*: IEEE press, 2000.

[41] J. Lyu, X. Cai, and M. Molinas, "Optimal design of controller parameters for improving the stability of MMC-HVDC for wind farm integration," *IEEE Journal of Emerging and Selected Topics in Power Electronics*, vol. 6, no. 1, pp. 40-53, 2017.

[42] Y. Wang, C. Zhao, and C. Guo, "Comparison study of small-signal stability of MMC-HVDC system in different control modes," *International Journal of Electrical Power & Energy Systems*, vol. 111, pp. 425-435, 2019.